Rakenteiden Mekaniikka (Journal of Structural Mechanics)
Vol. 56, No. 4, 2023, pp. 179–198
https://rakenteidenmekaniikka.journal.fi/index
https://doi.org/10.23998/rm.132039
© 2023 The Authors
Open access under the license CC BY 4.0

VERTAISARVIOITU
KOLLEGIALT GRANSKAD
PEER-REVIEWED
www.tsv.fi/tunnus

Feasibility and optimization of a bush-cut aluminium bronze big end bearing: a simulation-based study

Sami Kreivi[1], Teemu Kuivaniemi, Antti Mäntylä, Joona Vaara, Jaakko Istolahti, Pasi Halla-aho, Antti-Jussi Vuotikka and Tero Frondelius

Summary The big end bearing of a connecting rod is one of the most highly loaded bearings in marine engines. This paper presents a feasibility study and optimization of the geometrical parameters of a bush-cut bronze bearing for connecting rods in large-bore marine engines. An accurate simulation workflow was developed and carried out in Abaqus to analyze whether a new simple and cost-saving alternative for manufacturing big end bearings would be possible. The simulations showed that aluminium bronze is feasible regarding stress and yielding. However, improvements were needed to increase the radial contact pressure and decrease the compressive tangential stress peaks on the ends of the split bearing. The optimized design parameters included the outer diameter and thickness of the bearing, the thickness of the cutting blade, and the cut angle. Especially the combination of optimized blade thickness and cut angle generated promising results. The findings of this study provide valuable insights and design principles for bearing design processes.

Keywords: connecting rod, bearings, aluminium bronze, finite element method, simulation

Received: 14 August 2023. Accepted: 22 December 2023. Published online: 29 December 2023.

In memory of DSc Djebar Baroudi and Lic Jari Laukkanen

Introduction

The main component under study in this research paper is the big end bearing, which connects the connecting rod to the crankshaft. To gain a bigger picture of the entire connecting rod assembly, the conventional purposes, properties, and materials of its components are described in this paper. The components can be divided into the connecting rod itself and the bearings which are fitted into it. In addition, the loads affecting the bearing on a running engine and the usual manufacturing methods for the studied components are referred to in these research papers [1–4]. Even though this paper discusses large-bore marine engines, the principal characteristics of these components are features that are common in combustion engines regardless of their size.

The simulation and calculation of connecting rods with a finite element method (FEM) [5] in Wärtsilä dates back to the early seventies [1]. The history and development of

[1]Corresponding author: sami.kreivi@gbw.fi

structural analysis and dynamics seen in articles by Frondelius et al. [1,6] show the great experience of Wärtsilä in this field. The knowledge on simulating connecting rods, as demonstrated in the studies by Göös et al. [2], Mäntylä et al. [3], and Bai et al. [4], has been a considerable advantage for this paper. These studies represent or have led to methods for simulating the pretension of connecting rod bolts [2], considering the machining of the big end bearing housing after pretightening in simulation [3], and obtaining realistic bearing loads from elastohydrodynamic analyses of multibody system simulation models [4]. Our prior experience in the company has made it possible to utilize some already-known beneficial methods in this study, as well as add some new, more elaborate methods that will be used in connecting rod analyses in the future.

The main research question was to study if aluminium bronze CuAl10Fe5Ni5 would be a feasible material for big end bearings in terms of its mechanical performance and manufacturing advantages compared to conventional materials. Another objective was to gain knowledge of how the bearing's geometric parameters, such as outer diameter, wall thickness, cutting blade thickness, and cut angle, affect the performance and behaviour of the big end bearing. The desirable factors in an optimized bearing design were set to sufficient radial contact pressure between bearing and housing with no zero-pressure areas on the contact, as well as minimal yielding and plastic deformation on the ends of the bearing halves. An additional goal of the study was to further develop simulation-based methods that could be utilized as a guideline in modeling and analyzing the behaviour of big end bearings in future studies, considering the initial stress state deriving from the excessive diameter, non-uniform crush height, and the effect of machining the housing in a pretightened state.

The connecting rod, which links the piston to the crankshaft and converts the alternating linear movement of the piston into the rotation of the crankshaft in a reciprocating combustion engine, is a critical component [7]. The connecting rod experiences complex motion and load cycles at every operating cycle of a running engine, making it one of the most highly stressed components [8]. The primary loading for the connecting rod is an alternating tension and compression along its longitudinal axis, resulting from the forces produced in the cylinder. Both connecting rod ends have bearings, usually shrink-fitted sliding bearings. The small end bearing joins the piston pin, and the big end bearing joins the crankshaft journal to the connecting rod. The connecting rod shaft may have a customized cross-section, such as I- or H-shaped, depending on the requirements [9]. The most common failure that occurs in connecting rods is caused by the inertial and direct forces that bend the rod perpendicularly to the axes of small and big end bearings. The number of connecting rod failures has decreased partly since the piston strokes have been shortened, leading to shorter and stiffer connecting rod designs that are less prone to bending fatigue failures [10].

In a large-bore marine engine connecting rod, there are typically two big end halves and an upper part due to the large overall size of the assembly (see Figure 6). In this three-piece connecting rod design, the upper and lower parts are connected to the middle part with bolts, and, to ensure its cylindrical shape in a tightened state, the final machining of the big end housing is done after the pretightening of bolts. Otherwise, the big end housing might take an oval-like shape after pretightening, causing problems with big end bearing contact.

In this study, the focus was mainly on the connecting rod assembly of Wärtsilä 24 (W24) single-cylinder test engine. As a whole assembly, the connecting rod weighs about 65 kg and has a length of about 1000 mm. Connecting rods can be produced from

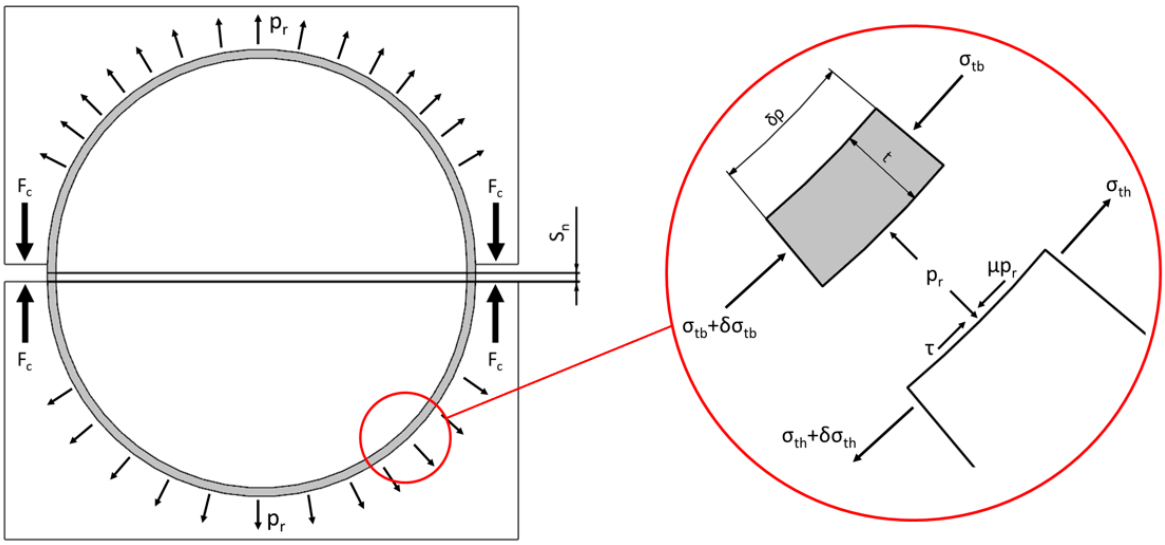

Figure 1. Crush height and loads on split-bearing design. F_c is clamping force, p_r is radial pressure, S_n is crush height, t is bearing shell thickness, δp is angle of cut out section, μ is coefficient of friction, σ_{tb} is tangential stress on bearing, $\delta\sigma_{tb}$ is difference of tangential stress on bearing through cut out section, σ_{th} is tangential stress on housing, $\delta\sigma_{th}$ is difference of tangential stress on housing through cut out section and τ is tangential stress caused by friction. [9]

various materials depending on the characteristics and resultant loads of the application. Commonly used materials include aluminium, steel, or alloy forgings [7]. The connecting rod material of the studied assembly was 42CrMo4, a quenched and tempered steel.

In internal combustion engines, plain journal or sliding bearings are commonly used between the shafts and the bearing housings [8]. These bearings have good shock resistance and damping properties, require low space, and are resilient to grime. They are also easy to assemble around shafts and have lower costs compared to rolling bearings. However, plain bearings have a higher friction level, leading to higher oil requirements [9].

The small and big end bearings of the connecting rod are also sliding bearings. The bearings are mounted to the small and big end eyes with shrink fit, ensuring that the bearing stays in place under running engine conditions. The sufficient shrink fit provides the needed radial pressure between the bearing and housing without resulting in high tangential stresses along the bearing shell, which could cause significant plastic deformations [9]. The split-bearing design is necessary for the big end of the connecting rod to assemble the bearing journal around the crankshaft. The manufacture of these split-bearing shells is usually done by specialized organizations that provide advice regarding the material and dimension selection of the bearing shells [8]. The split-bearing shells are clamped in place by tightening the bolts, creating a clamping force and preventing the bearing from spinning. Crush height (see Figure 1) is a critical design parameter for split bearings, as it affects the contact pressure and prevents fretting wear or collapse of the bearing shell [11].

The big end bearings examined in this study are relatively large, and there are more detailed features in the split-bearing design in addition to crush height. When the bearing shells are fitted into housing halves, the ends of the bearing shells bend inwards due to the shrink fit, resulting in a significant angle between the inner and outer edges of the bearing shell end. This angle has a great local effect on the outward force, tangential

stress, contact pressure, and yield [11].

The magnitude and direction of the forces that load the connecting rod bearings can be calculated as a function of the crank angle. Figure 2 represents an example of the big end bearing forces during a full cycle of an in-line marine engine. Connecting rod bearings experience loading resulting from gas and mass forces in cycles as the crankshaft revolves [11].

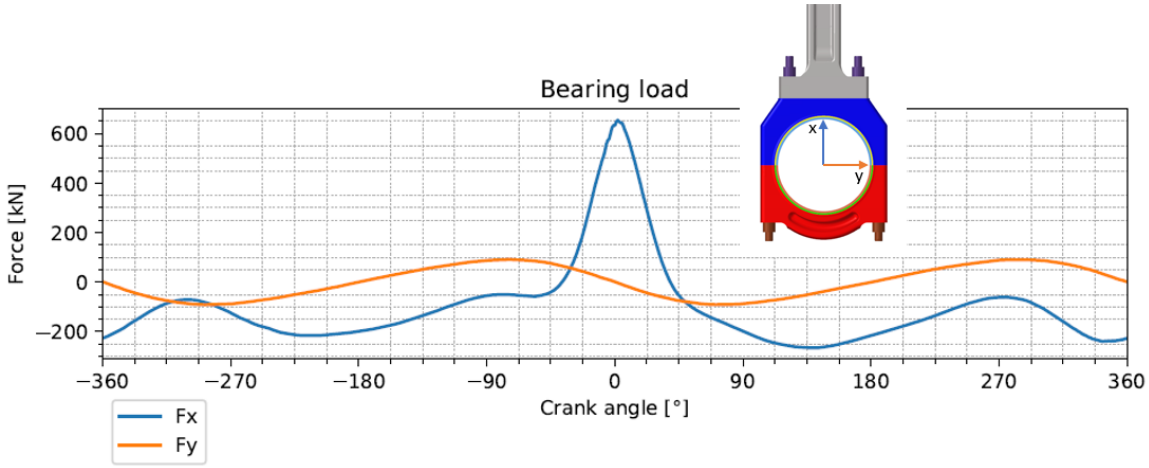

Figure 2. Bearing load of W25 marine engine as a function of crank angle related to top dead center.

Connecting rod bearings are exposed to high-cycle loading, contact with the oil film and metal-to-metal contact, temperature variations, water vapor, and acidic products from combustion. The selection of bearing materials is driven by factors such as fatigue strength, scuff resistance, wear rate, coefficient of thermal expansion, corrosion resistance, and machinability [12].

Bearing materials in reciprocating engines can be categorized into three groups: steel and babbitt metals, aluminium alloys, and copper alloys. Connecting rod bearings commonly use steel-backed precision inserts with bronze, babbitt, or aluminium as the bearing material to achieve sufficient strength and good tribological properties on the contact surface [13]. Copper alloys, especially bronzes, are increasingly used in bearings as they meet the requirements of many applications. Leaded bronze, for example, can be used in various conditions by adjusting the lead and tin content, resulting in different slip properties and material strength [9].

The conventionally used big end bearing in W24 connecting rod is a tri-metal steel-backed bearing with a lead bronze lining, which served as a comparison case for the newly proposed aluminium bronze bearing. Manufacturing process of this tri-metal bearing is much more complex and costly than the possibilities with a simpler bush-cut bearing.

Bush-cut aluminium bronze bearing

The new cost-saving manufacturing method of big end bearings by cutting a fully round bush in half was found promising for its simplicity, but various unknown factors on the applicability of the aluminium bronze CuAl10Fe5Ni5 as big end bearing material required a detailed study. In general, aluminium bronzes are copper-based alloys with 5 to 12 % of aluminium, and have high strength and excellent wear-resisting properties with a certain

concentration of alloying elements, which makes them one of the most versatile engineering materials [14]. The material had been formerly used as other bearings in marine engines, but not in the big end of connecting rod due to challenging requirements. Some principal mechanical and physical properties of the material are shown in Table 1.

Table 1. Mechanical and physical properties of CuAl10Fe5Ni5 [15].

	Sandcast	Centrifugally and continuously cast	Extruded/Rolled/ Forged
Density [kg/m^3]	7.6	7.6	7.6
Young's modulus [GPa]	110	110	110
Yield strength [MPa]	≥250	≥260	≥270
Tensile strength [MPa]	≥540	≥590	≥630
Elongation [%]	≥10	≥10	≥10
Hardness [HB]	≥140	≥150	≥170
Coefficient of thermal expansion (0 - 100 °C) [1/°C]	$16.5{\cdot}10^{-6}$	$16.5{\cdot}10^{-6}$	$16.5{\cdot}10^{-6}$
Thermal conductivity [W/(m·°C)]	65	65	65
Resistivity (20 °C) [nΩ·m]	190	190	190
Machinability	Good	Good	Good

To gain a sufficient crush height and radial pressure on the identical bearing halves when assembled to the housing, a slightly greater outer diameter of the plain bush than the diameter of the housing was chosen. As the cutting blade's thickness and the bearing's and housing's diameters are known, the analytical magnitude for crush height can be calculated with differences in circumferential lengths. The dimensions of the bearing and housing before mounting are illustrated in Figure 3 and after mounting in Figure 4. With a straight cut, the outer crush height will be slightly greater than the inner crush height.

To get equal crush heights on both the outer and inner edges of the bearing, an outwards opening cut angle would be needed. Due to that, an additional design parameter of an inwards or outwards opening cut angle was considered in the study. An illustration of bearing dimensions before mounting updated with cut angles can be seen in Figure 5.

Finite element model

All components of the finite element model of the connecting rod assembly were meshed with 10-node quadratic tetrahedral solid elements (C3D10 [16]) except the big end bearing halves UPPER_BEARING and LOWER_BEARING and a cylinder-like part of the big end housing contacting the bearing halves MIDDLE_PART2 and LOWER_PART2 that were meshed with 8-node linear brick solid elements with incompatible modes (C3D8I [16]). Hexagonal mesh was used in the most critical area of the study due to the need to gain accurate results with minimal numerical errors from the bearing halves and their contacts. Well-organized hexagonal mesh also enabled the convenient use of morphing and the collecting of results from straight paths. Component naming, element types, and a close-up of the hexagonal mesh are shown in Figure 6.

All analyses were run on Abaqus/Standard version 2020.HF2. The boundary condition used for the connecting rod assembly was a distributing coupling constraint. The reference node for the constraint was created on the center of gravity of the assembly and all its

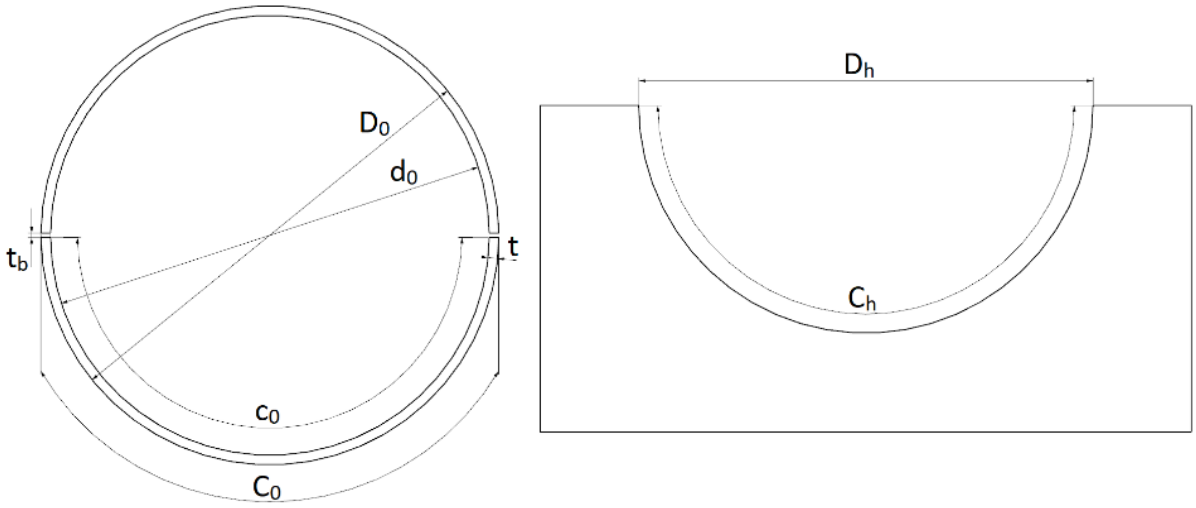

Figure 3. Dimensions of housing and bronze bearing before mounting.

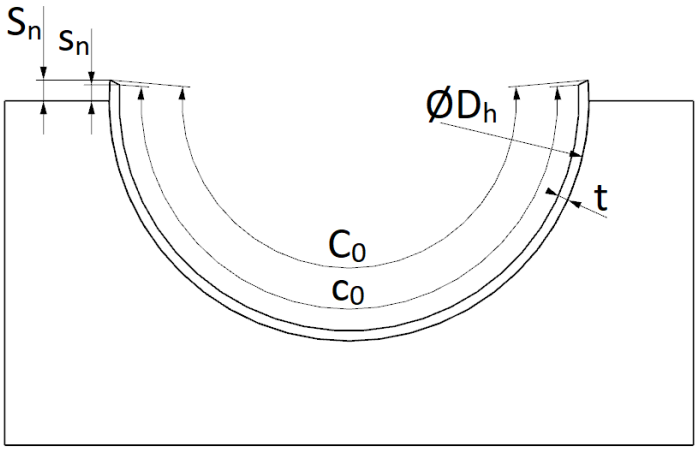

Figure 4. Dimensions of housing and bronze bearing after mounting.

degrees of freedom were constrained. Coupling nodes, chosen from surfaces on both sides of the UPPER_PART, were coupled to follow the average motion of the reference node in all degrees of freedom. However, deformation among these coupling nodes was allowed.

Used material models were elastoplastic with isotropic hardening since deeper knowledge of the material behaviour under compressive loading was unknown. Stress-strain relation after the yield limit was defined with either two or three points and a continuation with ideal plasticity, which resulted in a sufficient magnitude of plastic strains to make a comparison of certain phenomena between different analyses. Temperature-dependent material properties were not taken into account in this study.

The material properties for connecting rod steel 42CrMo4 BS EN10250, steel bearings C22 EN10250-2:2000 with lining G-CuPb22Sn DIN 1716, and connecting rod bolts were taken from corresponding standards. Young's modulus of steel bearings was defined as an equivalent considering the thickness of the lining material. Material definitions and their respective true stress-strain curves are shown in Figure 7.

Apart from plastic properties, other material properties for the new big end bearing material, aluminium bronze CuAl10Fe5Ni5, were collected from the WIAM MET-

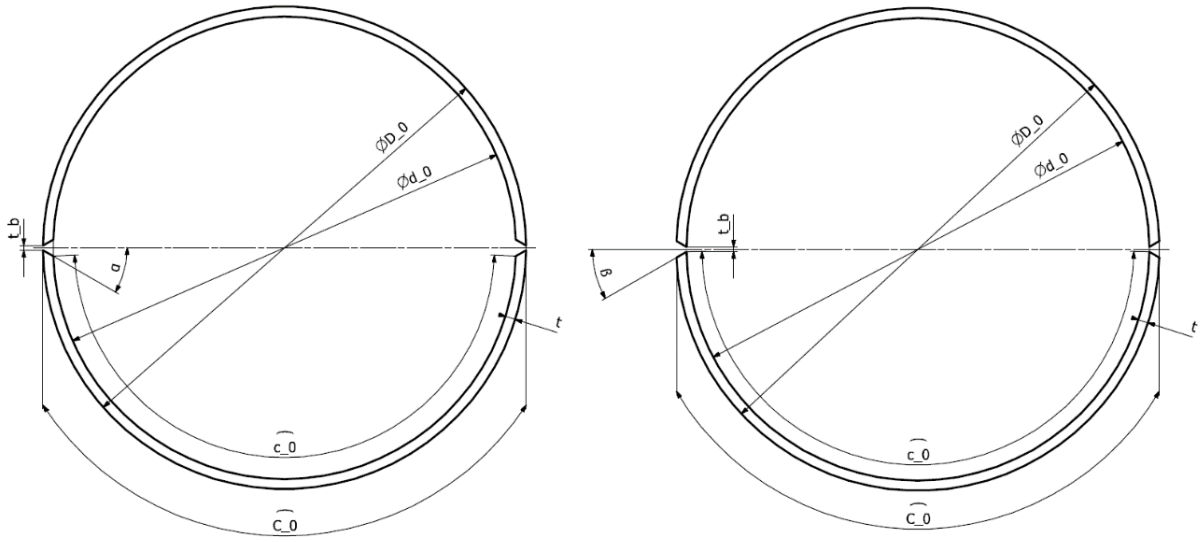

Figure 5. Bearing dimensions with cut angle.

ALLINFO materials database [17]. Yield limit and plastic stress-strain relations were obtained from the results of a tensile test performed by Oy Johnson Metall Ab. Definitions and the true stress-strain curve of the material model for bronze bearings are shown in Figure 8.

A compression test for aluminium bronze would have brought more detailed information about the material's behaviour under compressive loads, but for time limitations it had to be left for further studies. Priorly aluminium bronze CuAl10Fe5Ni5 has been modeled with different yield strengths under tension and compression [18], which would refer to a strength-differential phenomenon in the discussed material [19, 20]. The stress state of big end bearings tends to be mainly on the compressive side, so a difference in tensile and compressive strengths would probably have had an effect on the final results. A material model updated with a yield criterion that takes into account the difference between the yield strengths in both tension and compression, for example the Mises-Schleicher criterion [21, 22], would be worth studying in this application. For this simulation-based study, however, the plasticity properties obtained from tensile tests were concluded acceptable for the compressive stress states as well. Even if there is a strength-differential phenomenon in the material, it is known from the literature that the yield stress under tension is lower than under compression in metals [19, 20], which leads to results being slightly conservative.

Contact modeling was one of the most essential aspects of the simulations of this study. For example, the modeling of machining the big end housing in a pretightened state, friction definitions, interference fits, initial and variable clearances between surfaces, and interesting phenomena seen in the final results are connected to contact modeling. Contact pairs with friction and small sliding formulation were used everywhere else except between the cylindrical innermost part of the big end bearing housing and the rest of the housing, which was tied. Friction coefficient of 0.2 was used between the bearing ends and on the bolt contacts, whereas 0.1 was used on other contact pairs. Additionally, an elastic slip of 10^{-4} was defined for every contact pair. To get noise-free and accurate results from contacts with round geometry, adjusting secondary nodes in addition to surface smoothing functionality was used. Abaqus' surface smoothing improves the accuracy and robustness of contact computations by comparing the slightly angular meshed surface

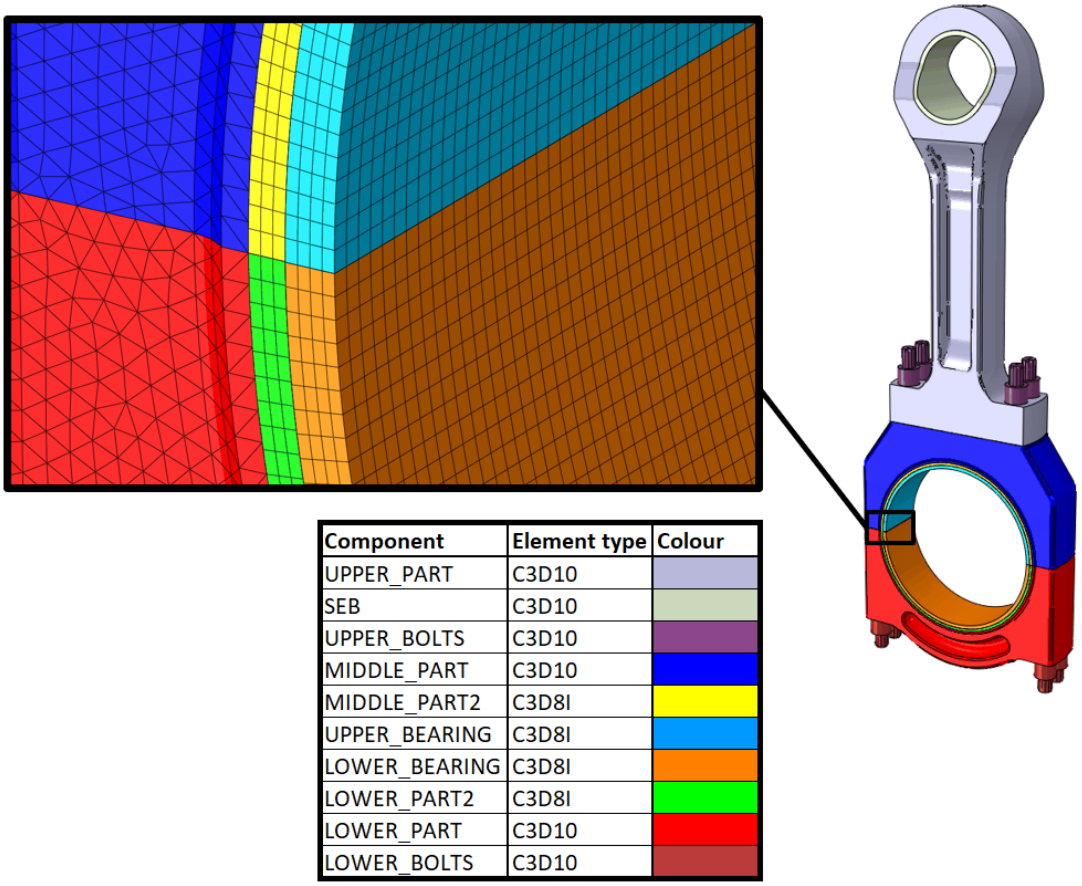

Component	Element type	Colour
UPPER_PART	C3D10	
SEB	C3D10	
UPPER_BOLTS	C3D10	
MIDDLE_PART	C3D10	
MIDDLE_PART2	C3D8I	
UPPER_BEARING	C3D8I	
LOWER_BEARING	C3D8I	
LOWER_PART2	C3D8I	
LOWER_PART	C3D10	
LOWER_BOLTS	C3D10	

Figure 6. Components and element types of the connecting rod assembly.

and a given idealized initial geometry of the same surface, whereas adjusting functionality moves the secondary nodes within a given tolerance value precisely on the primary surface, eliminating any unwanted initial overclosures or gaps in the contact [16].

Methodology

An essential part of this study was to find an accurate and realistic modeling method to study the significant phenomena of the big end bearing during the assembly and the maximum loading it may experience after manufacturing. These steps include pretightening the big end housings together with bolts, the first assembly of bearing halves to the big end housings, and adding the maximum mass and gas loads to the bearing. The main interest was to determine if the new aluminium bronze bearing material was feasible in this kind of location, as the big end bearing is the most complicated bearing in marine engines due to its split-bearing design and challenging loads in running conditions. The simulations were conducted using a multiphase approach, consisting of over 40 final simulation cases. The simulation workflow is illustrated in Figure 9.

The pretension simulation was the initial analysis of the assembly and loading simulation process. It involved pretightening the big end housing with connecting rod bolts and installing the small end bearing with a shrink fit. Pretension forces for the bolts were applied with pretension sections. These are cut surfaces on the bolts that are controlled by separate nodes loaded with concentrated loads [16]. Shrink fit of the small end bearing was modeled with a negative clearance value and contact interference functionality. Sep-

	Connecting rod
Density ρ	7.85 kg/m^3
Young's modulus E	206 GPa
Poisson's coefficient ν	0.3
Yield limit Y	500 MPa
Plastic strain ε_p (True stress σ)	0.002 Strain (550 MPa)
	0.14 Strain (800 MPa)
Elasticity and hardening	Isotropic

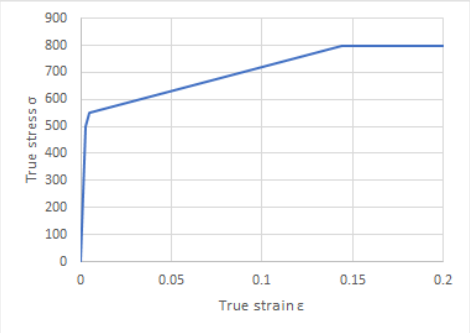

	Steel bearings
Density ρ	7.85 kg/m^3
Young's modulus E	193.145 GPa
Poisson's coefficient ν	0.3
Yield limit Y	350 MPa
Plastic strain ε_p (True stress σ)	0.002 Strain (400 MPa)
	0.2 Strain (550 MPa)
Elasticity and hardening	Isotropic

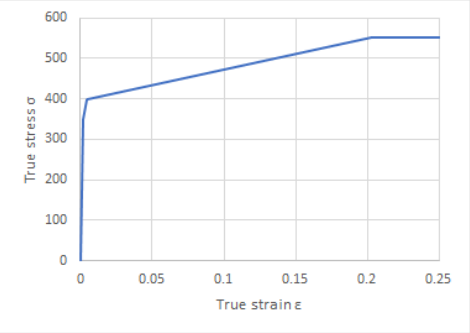

	Bolts
Density ρ	7.85 kg/m^3
Young's modulus E	206 GPa
Poisson's coefficient ν	0.3
Yield limit Y	1000 MPa
Plastic strain ε_p (True stress σ)	0.002 Strain (1050 MPa)
	0.1 Strain (1200 MPa)
Elasticity and hardening	Isotropic

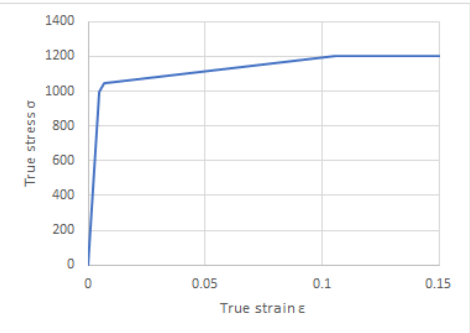

Figure 7. Material definitions and true stress-strain curve of connecting rod, steel bearings, and bolts.

arate analyses were performed for maximum and minimum interference fits of the big end bearing according to the tolerances. The big end bearing halves were not yet included in the analysis at this phase, because the pretightening of the bolts causes the big end housing to take a slightly oval-like shape (see Figure 10) which needs to be machined back to a perfectly round shape.

To accurately capture the stress state of the big end bearing halves during assembly, a separate free spread simulation was conducted to determine the initial stress field resulting from their excessive diameter. This analysis involved applying a prescribed displacement to the ends of the bearing halves, considering the difference between the diameters of the bearing and housing. The results of this analysis matched very well with some more realistically simulated analyses of fitting bearing halves into housing, which again were validated with strain gauge measurements of steel bearings in the same kind of fitting event [23]. The good correlation of results from fitting measurements, realistic fitting simulations, and simple free spread simulations led to the decision to use this much simpler simulation method.

The assembly simulation of the big end bearing included the effects of machining the

	Bronze bearings
Density ρ	7.6 kg/m^3
Young's modulus E	124 GPa
Poisson's coefficient ν	0.32
Yield limit Y	233 MPa
Plastic strain ε_p (True stress σ)	0.0001 Strain (245 MPa)
	0.002 Strain (316.5 MPa)
	0.02 Strain (445.6 MPa)
Elasticity and hardening	Isotropic

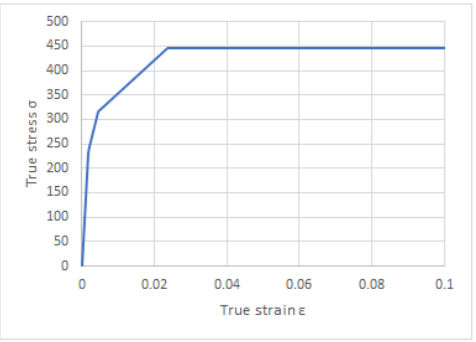

Figure 8. Material definitions and true stress-strain curve of bronze bearings.

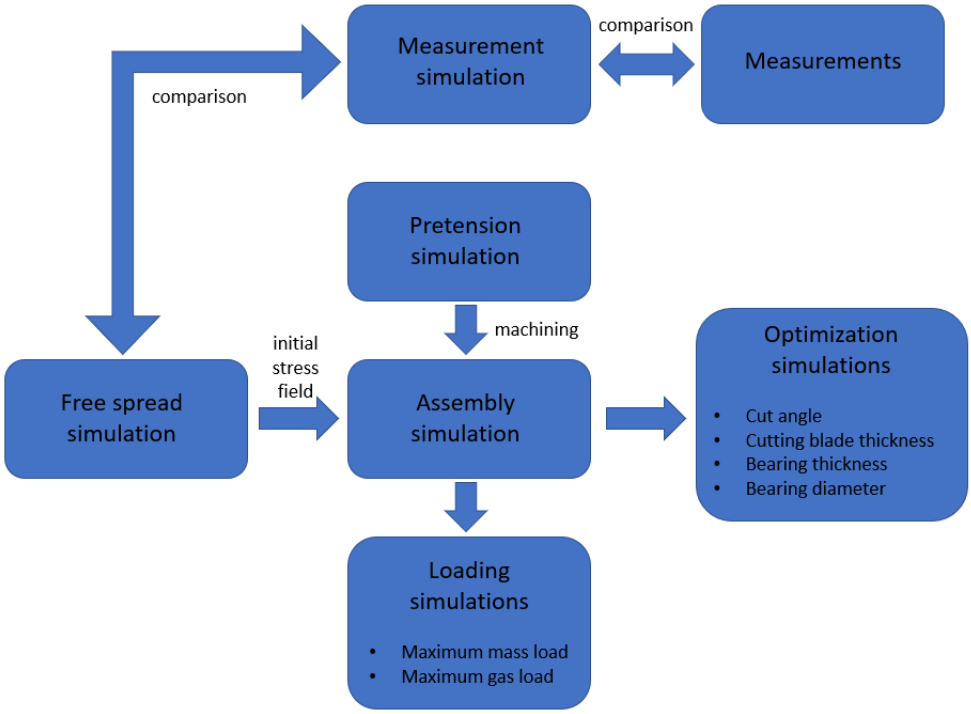

Figure 9. Simulation workflow.

big end housing in a pretightened state, the initial stress field of the bearing halves, and the crush height resulting from the circumferential overlength of the bearing. The effect of machining was simulated by importing the connecting rod assembly without the bearing halves from the pretension step, in its already developed state, and the bearing halves were included in the model intact. In addition, the surface smoothing functionality with adjusting was used to shape the housing's ovality into perfect roundness. This method moved the nodes on the housing surface to match the nodes of the bearing halves without changing their stress-strain state. The stress field of bearing halves developed in free spread simulation was included in the assembly analysis as the initial stress field of the bearing halves. With this method, the load histories of both the bearing halves and the rest of the assembly were included in the analysis. Especially in plasticity theory the strains are affected by the whole history of loading [24], and as plasticity of the new bearing was one of the main factors under research, this update to the simulation process was required. Additionally, the crush height of the bearing halves was precisely defined

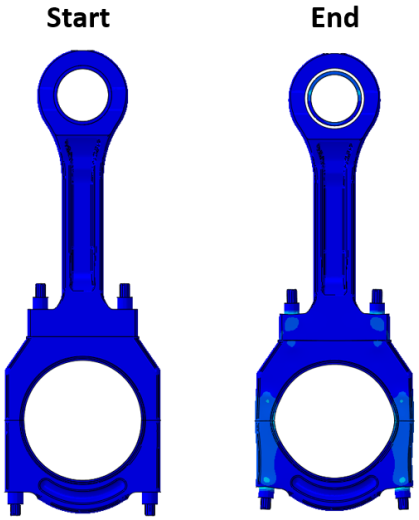

Figure 10. Deformation of the big end housing and shrink fit of the small end bearing during pretension step (scale factor = 100).

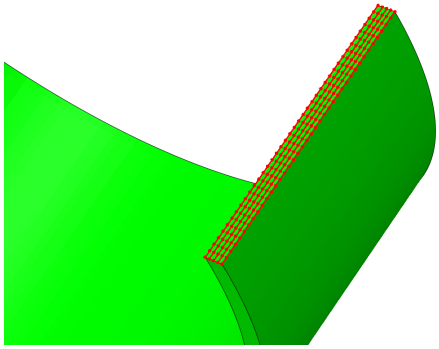

Figure 11. Five node rows at the bearing end for crush height definition.

as analytically calculated negative clearance in a tabular form respective for every node row between the bearing ends (see Figure 11) and simulated with contact interference functionality. The simulations were again performed for both steel and bronze bearings with different interference fits. The results of the assembly simulations provided insights into the behaviour of the bearing during assembly, including the development of contact pressure, tangential stress around the bearing, plastic deformation, and the bending of bearing ends. A better understanding of the development of the bearing's stress state between mounted and assembled state can be established from Figure 12. When the housings are tightened against each other with bearing halves between them, the small inward-opening angle deriving from a straight cut and excessive diameter at the bearing ends "straightens" as the bearing is pressed against the housing due to the crush height. This leads to the situation that the bearing ends slightly bend outwards against the housing, creating a high compressive stress peak at the inner edge and a zero-pressure area on the outer surface near the ends.

The loading simulations aimed to verify the feasibility of bronze bearings under maximum mass and gas loads. The final state of the assembly analysis was imported and the bearing's inner surfaces were loaded with distributed loads. Mass and gas loads were exported as elastohydrodynamic pressures from multibody dynamics and elastohydrodynamic analyses for the same engine. The results of these simulations confirmed that the bronze bearings exhibited acceptable stress levels and the plastic deformation did not increase under the maximum loading conditions of the engine cycle (see Figure 2). Von Mises stresses on circumferential paths around the bearing on inner and outer surfaces from the center (C2) and maximum width (C1) under maximum mass and gas loads can be seen in Figure 13. From the stress range in these results, it can also be concluded that the plastic material model of aluminium bronze is sufficient for these simulations.

Based on the assembly and loading simulations, it was concluded that the use of aluminium bronze as a big end bearing material was possible from the stress and yield point of view. Further optimizations were conducted to improve the bearing design, such as eliminating stress peaks at the bearing ends, minimizing zero-pressure areas on the contact with housing, increasing uniformly distributed radial contact pressure, and

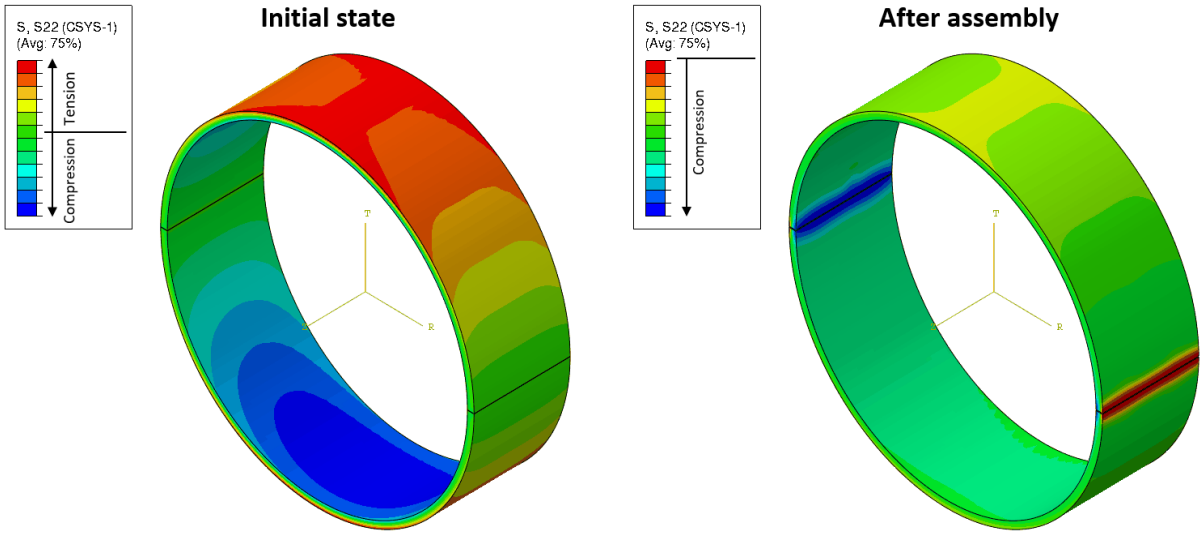

Figure 12. Tangential stress of bearing in cylindrical coordinate system before and after assembly.

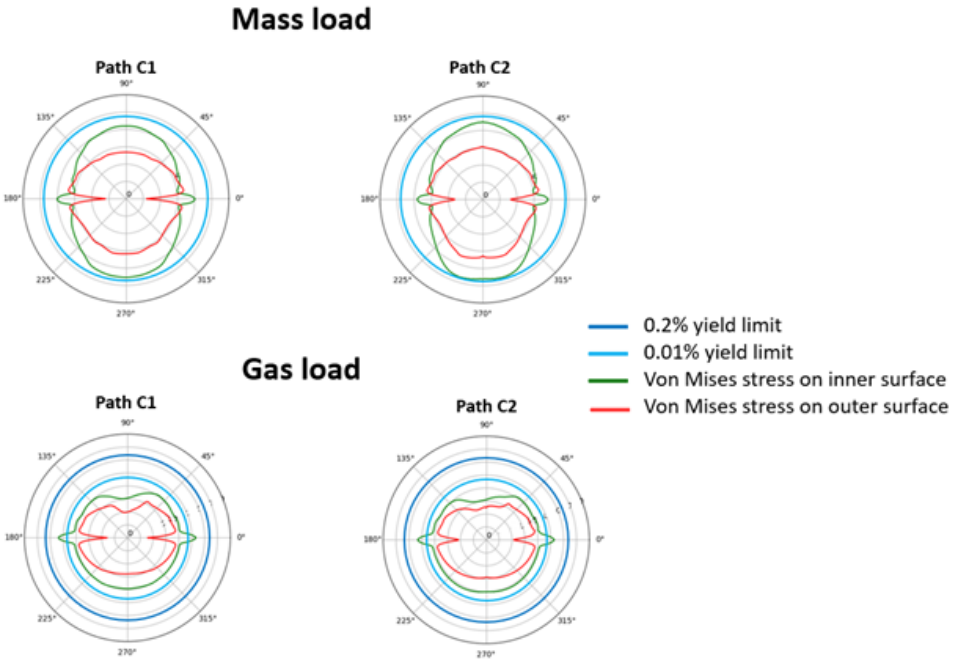

Figure 13. Von Mises stresses on circumferential paths around bearing under loading.

understanding the sensitivities of geometric parameters of the bearing in assembled state.

Sensitivity study of geometric parameters

Geometrically, a sliding bearing is rather simple: it is basically a hollow cylinder with known inner and outer diameters, wall thickness and width. Even as a split-bearing, the additional geometric variables are the thickness of cutting blade and if the cut is straight or at a certain angle. These parameters do, however, have a considerable effect on different phenomena when the bearing is tightened into housing with an excessive outer diameter and crush height.

An Excel-tool was created and utilized solely for the purpose of calculating bearing

dimensions in an assembled state if the dimensions before mounting are known. Bearing thickness t, bearing outer diameter D_0, housing diameter D_h, cutting blade thickness t_b, and the inwards α and outwards β opening cut angles were used as inputs in this calculation tool. The circumferential lengths of the outer C_0 and inner c_0 edges of the bearing halves after cutting the bush were first calculated as

$$C_0 = \frac{\pi \cdot D_0}{2} - t_b - 2 \cdot \tan \frac{\pi \cdot \beta}{180^\circ} \cdot t, \tag{1}$$

$$c_0 = \frac{\pi \cdot (D_0 - 2 \cdot t)}{2} - t_b - 2 \cdot \tan \frac{\pi \cdot \alpha}{180^\circ} \cdot t. \tag{2}$$

The circumferential lengths were then utilized in calculating the crush heights on the outer S_n and inner s_n edges of the bearing as

$$S_n = \frac{D_h}{4} \cdot \sin \frac{2 \cdot C_0 - \pi \cdot D_h}{D_h}, \tag{3}$$

$$s_n = \frac{D_h - 2 \cdot t}{4} \cdot \sin \frac{2 \cdot c_0 - \pi \cdot (D_h - 2 \cdot t)}{D_h - 2 \cdot t}. \tag{4}$$

Finally, the crush heights were calculated to five equally spaced node rows along bearing thickness (see Figure 11) by the following equation

$$S_i = s_n + (i - 1) \cdot \frac{S_n - s_n}{4}, \tag{5}$$

where i = 1, 2, ... is the node row number starting from the innermost edge and S_i is the crush height on the node row i. Radial interference between the bearing and the housing can be simply calculated as $(D_h - D_0)/2$. See figures 3, 4 and 5 for illustrated bearing and housing dimensions.

The geometric parameters studied to gain an optimized bronze bearing geometry were outer diameter and wall thickness of the bush, cutting blade thickness, and the cut angle. Every simulation in this sensitivity study was run like the assembly simulations, modifying only the big end bearing geometry, and was compared to the results of the original assembly simulation. In the next paragraphs, the modeling methods and the primary effects of modified geometric parameters are shortly presented.

Varying outer diameters for the bearing bush were modeled by executing the free spread simulations and changing the crush height value for each diameter. The most significant change in results with a larger outer diameter was the increased bending due to free spread. The increased bending enlarges the difference of tangential stress between the outer and inner surfaces on the middle point of bearing halves, far from the ends. A 0.04 % increase in diameter led to a 4.3 % greater difference in tangential stress and a 0.2 % increase led to a 23.3 % greater difference as illustrated in Figure 14. As the whole bearing will be under compressive tangential stress after assembly, the initial tensile tangential stress on the outer surface will relieve and the initial compressive tangential stress on the inner surface will magnify the overall stress state after assembly.

The varying wall thickness of the bearing was modeled by changing only the inner diameter of the bush by morphing the mesh. Bearings with 18.9 % thicker and thinner wall thicknesses were compared to the original geometry. With a thicker bearing bush, the most significant effect was the increase in average radial contact pressure between the

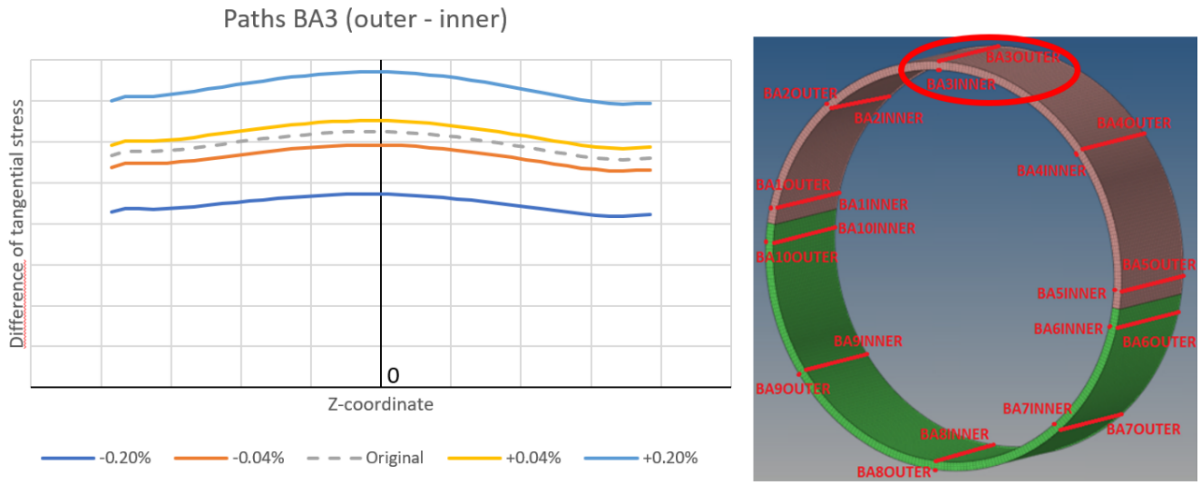

Figure 14. Difference of tangential stress on path BA3 with different outer diameters.

Table 2. Average contact pressures with different bearing thicknesses relative to original bearing design.

	Relative average contact pressure [%]		
Bearing thickness	Bearing ends	Upper bearing	Lower bearing
-18.9 %	100.98	81.48	81.25
Original	100	100	100
+18.9 %	98.38	117.28	116.25

bearing and the housing and a slight decrease in average contact pressure between bearing ends (see Table 2).

Modifying the cutting blade thickness had a direct effect on the crush height, which is one of the most essential dimensions in a split bearing. Naturally, a thinner cutting blade leads to a higher crush height and vice versa. The main effects of a thinner cutting blade were a higher contact pressure between the bearing and housing and between bearing ends, and a higher average compressive tangential stress throughout the bearing. A 2 % thinner cutting blade resulted in roughly 7 - 8 % higher average contact pressures (see Table 3) and average compressive tangential stresses. These factors increased the plastic deformation at the bearing ends as well. The equivalent plastic strain at the inner edge of bearing ends increased 35.6 % with a 2 % thinner and decreased 34.4 % with a 2 % thicker cutting blade from the original 0.07% Strain as seen in Figure 15.

Table 3. Average contact pressures with different blade thicknesses relative to original bearing design.

	Relative average contact pressure [%]		
Blade thickness	Bearing ends	Upper bearing	Lower bearing
+2 %	92.78	92.59	92.5
Original	100	100	100
-2 %	107.37	107.41	107.5
-4 %	114.83	114.81	115

The cut angle was taken into account in crush height definition, as the interference

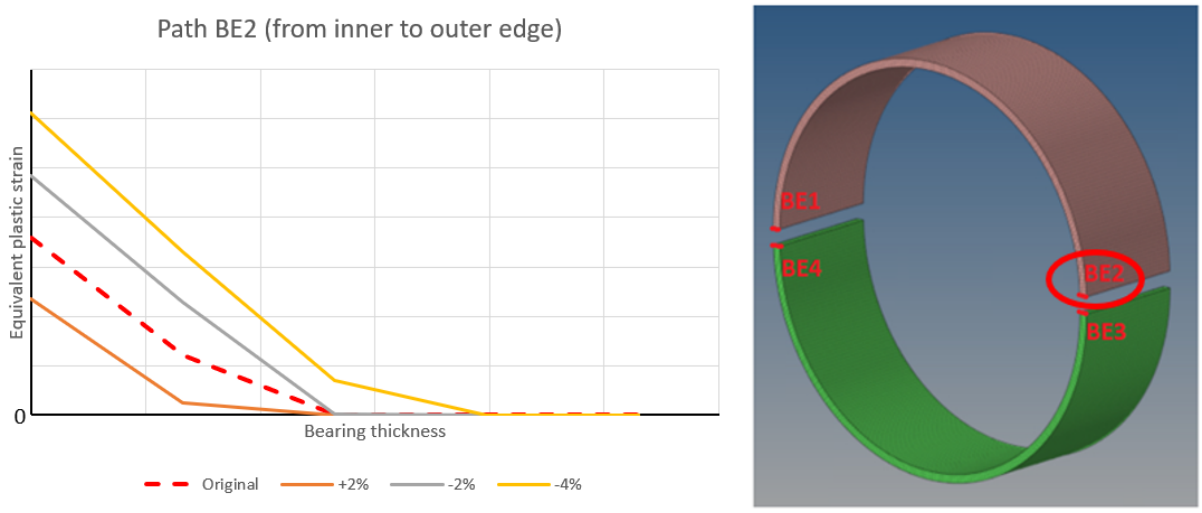

Figure 15. Equivalent plastic strain on path BE2 with different cutting blade thicknesses.

magnitude could be analytically calculated with the before-mentioned Excel-tool and defined for every node row at the bearing ends separately. Several experiments were done with both inwards and outwards opening cut angles of different sizes, but the most remarkable improvements in bearing results were reached with rather small, less than 0.25°, inwards opening angles. The most significant improvements with an optimal inwards opening cut angle were seen in minimized zero-pressure area in the contact between the bearing and housing near the bearing ends, as well as in the elimination of stress peaks and plasticity at the bearing ends. Although the selection of an optimal cut angle turned out to demand great precision, the quality-enhancing effects of the target variables with it led to a more detailed examination.

Especially the minimization of the zero-pressure area in bearing contact was a desired improvement, as it would decrease the possibility of fretting, which had occurred in the very same location earlier. Fretting may occur from solid bodies slipping against each other and it significantly reduces the fatigue properties of materials, as cracks are prone to initiate from fretting wear on contact surfaces [25]. Nevertheless, a more detailed fretting study with QT-steel housing and aluminium bronze bearing would be needed to verify the possibility of using this contact pair in the big end, as earlier studies have shown aluminium bronze to decrease the fretting fatigue life in different sets of conditions [26,27].

Optimized cut angle and cutting blade thickness

The cut angle and cutting blade thickness were detected to be the most significant optimization parameters, as they would bring the sought features into bearing results. Due to that, a bronze bearing with a combination of a 2 % thinner cutting blade and an optimal small inwards opening cut angle was simulated. The average compressive tangential stress with this optimized geometry is roughly 6 % higher on the whole bearing, but the stress peaks at the inner edges of bearing ends are decreased by 17 %, which is already under the initial yield limit of aluminium bronze. As seen in Figure 16, a much smoother tangential stress distribution is achieved in assembled state with the optimized geometry.

The elimination of stress peaks at the bearing ends on optimized geometry significantly decreases the plasticity, resulting in even 75 % lower maximum plastic strains. A comparison plot of equivalent plastic strain at the bearing ends of the original and opti-

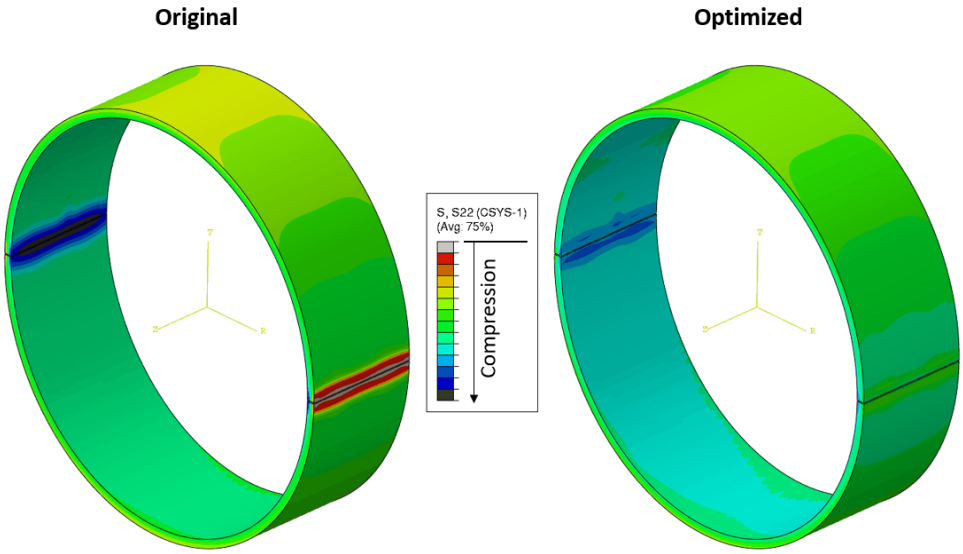

Figure 16. Tangential stress distribution in cylindrical coordinate system with original and optimized design.

mized design can be seen in Figure 17. In Figure 18 it can be noticed that the contact pressure on the outer surface reaches much closer to the bearing ends in the optimized design. The zero-pressure area is minimized by at least 50 % with a thinner cutting blade and an optimal cut angle.

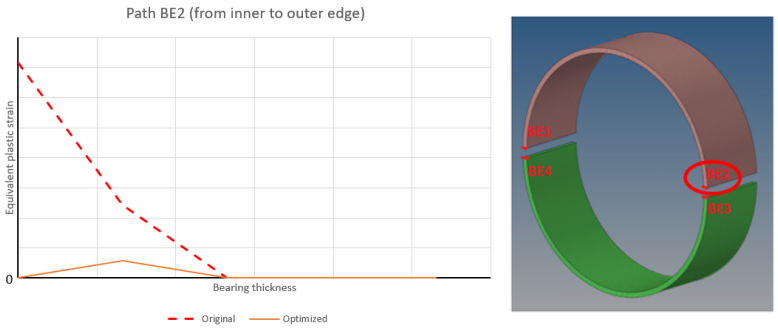

Figure 17. Equivalent plastic strain on path BE2 in original and optimized design.

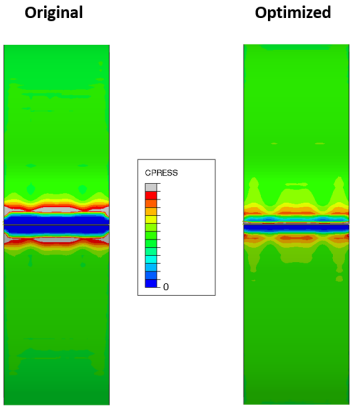

Figure 18. Contact pressure distribution in original and optimized design.

Table 4. Average contact pressures with original and optimized bronze bearing relative to conventional steel bearing.

		Relative average contact pressure [%]		
		Bearing ends	Upper bearing	Lower bearing
Steel	Maximum interference	100	100	100
Bronze	Maximum interference	87.87	87.10	87.91
Bronze	Optimized	95.34	94.62	92.31

In addition, the average radial contact pressure is increased by approximately 7 % in the optimized design, which in other words is over 90 % of the contact pressure in conventional steel-back bearing with maximum interference according to manufacturing tolerances (see Table 4). Eventually, the combination of a thinner cutting blade and a small inwards opening cut angle fulfilled the optimization objectives. Radial contact pressure between bearing halves and housing was increased, zero-pressure areas in contact were minimized and the stress peaks and plastic deformation at the bearing ends were eliminated. Additionally, the results of optimizing the bearing design with these parameters are highly local and would not have any negative effects on any adjacent components of the engine. More importantly, knowledge of the phenomena and effects of different geometric parameters with their sensitivities was gathered to be utilized in further design processes.

Conclusions

The main objective of this study was to discover if aluminium bronze would be feasible as a big end bearing material through a simulation-based study. Aluminium bronze was studied due to possible savings in manufacturing costs and because of its simple manufacturing method, where two identical bearing halves are gained by cutting a bush in half. The material had already been used in other bearings, for example in small end of the connecting rod, but not as the most highly loaded big end bearing.

The studied connecting rod assembly was from the Wärtsilä 24 single cylinder engine, and the compared bearings were the conventional tri-metal steel backed and the new bush-cut aluminium bronze bearing, both examined with their maximum and minimum interference fits. A generally applicable and accurate simulation method for bearings was developed further. The calculation model and simulation methods were validated with strain gauge measurements and the measured and simulated results of the steel bearing correlated well. This led to the conclusion that the new simulation methods could be used as a guideline in future bearing calculations at Wärtsilä. Based on the simulations with both big end bearing materials, the aluminium bronze bearing seemed to be feasible in terms of stress and yielding. However, some improvements were needed to increase radial contact pressure and eliminate the stress peaks that caused plastic deformation at the bearing ends. As the bearing was tightened in the housing, a compressive tangential stress peak could be noticed on the inner edges of the bearing ends and a zero-pressure area on the contact between the bearing and housing near the ends occurred.

Another task was to study the effects of modifying different geometric parameters of the bearing and finally optimize the geometry of the bronze bearing in the studied connecting rod assembly. The geometric parameters in the sensitivity study were the outer diameter and thickness of the bearing, the thickness of the blade used in cutting the bush, and a possible cut angle as an alternative to a straight cut. The sensitivities of different parameters to bearing behaviour were collected and presented with relative values to the original design and conventional steel bearing. The most promising results were obtained by using a 2 % thinner cutting blade and an optimized, less than 0.25°, inwards opening cut angle. With these modifications, a desired radial contact pressure was reached with approximately a 7 % increase, stress peaks and yielding at the bearing ends were minimized to cause 75 % less plastic strain, and the zero-pressure area near the bearing ends on the contact between the bearing and the housing was reduced in half. So small of a cut angle demands high but possible machining accuracy, but taking into

account the benefits it could lead to, it is worth taking into more detailed examination and experimental tests. The minimization of the zero-pressure area in bearing contact, especially to decrease fretting possibility, has been a goal for a long time. Even though some further studies, for example fretting analysis and simulations with a more accurate material model, are needed to ensure the feasibility of aluminium bronze as a big end bearing material, from the stress and yield point of view it is highly possible. Additionally, the knowledge and understanding of the phenomena in bearings gained from the optimization study resulted in generally applicable design principles in the bearing design process.

Acknowledgement

Co-funded by the European Union (Grant Agreement No. 101058179; ENGINE). Views and opinions expressed are however those of the authors only and do not necessarily reflect those of the European Union or the European Health and Digital Executive Agency. Neither the European Union nor the granting authority can be held responsible for them.

References

[1] T. Frondelius, M. Haataja, and H. Tienhaara. History of structural analysis & dynamics of wärtsilä medium speed engines. *Rakenteiden Mekaniikka (Journal of Structural Mechanics)*, 51(2):1–31, 2018. URL: https://doi.org/10.23998/rm.69735.

[2] J. Göös, T. Frondelius, A. Leppänen, and A. Mäntylä. Large bore connecting rod simulations. *Rakenteiden Mekaniikka (Journal of Structural Mechanics)*, 50(3):275–278, 2017. URL: https://doi.org/10.23998/rm.64658.

[3] A. Mäntylä, T. Frondelius, J. Göös, and A. Leppänen. Large bore connecting rod fretting analysis. *Rakenteiden Mekaniikka (Journal of Structural Mechanics)*, 50(3):239–243, 2017. URL: https://doi.org/10.23998/rm.64914.

[4] L. Bai, T. Frondelius, P. Halla-aho, and T. Kuivaniemi. Elastohydrodynamic simulation of the slider bearing. *Rakenteiden Mekaniikka (Journal of Structural Mechanics)*, 50(3):283–286, 2017. URL: https://doi.org/10.23998/rm.64922.

[5] J. Könnö and R. Stenberg. Non-conforming finite element method for the brinkman problem. In *Numerical Mathematics and Advanced Applications 2009*, pages 515–522, Berlin, Heidelberg, 2010. Springer, Berlin, Heidelberg. URL: https://doi.org/10.1007/978-3-642-11795-4_55.

[6] T. Frondelius, M. Haataja, J. Kömi, and H. Tienhaara. Simulation-driven development of combustion engines: Theory and examples. *SAE Technical Paper*, (2018-01-5050):14, 2018. URL: https://doi.org/10.4271/2018-01-5050.

[7] W. W. Pulkrabek. *Engineering Fundamentals of the Internal Combustion Engine*. Pearson Prentice-Hall, Upper Saddle River, NJ, second edition, 2004.

[8] C. F. Taylor. *The Internal-Combustion Engine in Theory and Practice*, volume 2. MIT Press, Cambridge, MA, revised edition, 1985.

[9] R. Van Basshuysen and F. SchÃ¤fer. *Internal Combustion Engine Handbook: Basics, Components, Systems and Perspectives*. SAE International, Warrendale, PA, 2004.

[10] D. H. Wright. *Testing Automotive Materials and Components*. Society of Automotive Engineers, Warrendale, PA, 1993.

[11] K. L. Hoag. *Vehicular engine design*. SAE International, 2006.

[12] M. Airila, K. Ekman, P. Hautala, S. Kivioja, M. Kleimola, H. Martikka, J. Miettinen, E. Niemi, A. Ranta, J. Rinkinen, P. Salonen, A. Verho, M. Vilenius, and V. Välimaa. *Koneenosien suunnittelu*. WSOY, 4 edition, 2003.

[13] J. B. Heywood. *Internal Combustion Engine Fundamentals*. McGraw-Hill, 1988.

[14] Y. Li, T. L. Ngai, and W. Xia. Mechanical, friction and wear behaviors of a novel high-strength wear-resisting aluminum bronze. *Wear*, 197(1):130–136, 1996. URL: https://doi.org/10.1016/0043-1648(95)06890-2.

[15] Johnson Metall. Copper alloy, JM7, CuAl10Fe5Ni5-C. URL: https://www.johnson-metall.com/img/file.php?id=75879, 2021. Accessed: 4 April 2021.

[16] Dassault Systêmes. SIMULIA User Assistance 2020 – Abaqus. URL: https://help.3ds.com/2020/English/DSSIMULIA_Established/SIMULIA_Established_FrontmatterMap/sim-r-DSDocAbaqus.htm?ContextScope=all&id=9a5d7bf209394446819332b397a93f40#Pg0, 2020. Accessed: 27 July 2021.

[17] IMA Dresden. WIAM® METALLINFO Criteria of Choice. URL: www.wiamonline.de/wiamdb/auswahl.php, 2021. Accessed: 27 July 2021.

[18] J. Jankowski, D. Kołakowski, and B. P. Pisarek. Analysis of mechanical and thermal stresses in a pressure casting machine plunger. *Advances in Science and Technology Research Journal*, 14(1):209–223, 2020. URL: https://doi.org/10.12913/22998624/117724.

[19] J. P. Hirth and M. Cohen. On the strength-differential phenomenon in hardened steel. *Metallurgical Transactions*, 1(1):3–8, 1970.

[20] D. C. Drucker. Plasticity theory, strength-differential (SD) phenomenon, and volume expansion in metals and plastics. *Metallurgical Transactions*, 4(3):667–673, 1973.

[21] F. Schleicher. Der spannungszustand an der flieÃŸgrenze (plastizitÃ¤tsbedingung). *Zeitschrift für angewandte Mathematik und Mechanik*, 6(3):199–216, 1926.

[22] J. Lubliner. *Plasticity theory*. Macmillan, 1990.

[23] S. Kreivi. Feasibility study and optimization of a bush cut bronze bearing for connecting rods in marine engines. Master's thesis, University of Oulu, 2021. URL: http://urn.fi/URN:NBN:fi:oulu-202110209162.

[24] J. Chakrabarty. *Theory of plasticity*. McGraw-Hill, 2 edition, 1987.

[25] D. A. Hills. Mechanics of fretting fatigue. *Wear*, 175(1):107–113, 1994.

[26] J. Hintikka, A. Lehtovaara, and A. Mäntylä. Fretting fatigue and friction of quenched and tempered steel in dry contact with aluminum bronze. *Wear*, 308(1–2):155–165, 2013. URL: https://doi.org/10.1016/j.wear.2013.07.002.

[27] W. Ren, S. Mall, J. H. Sanders, and S. K. Sharma. Evaluation of coatings on Ti-6Al-4V substrate under fretting fatigue. *Surface & Coatings Technology*, 192(2):177–188, 2005. URL: https://doi.org/10.1016/j.surfcoat.2004.07.084.

Sami Kreivi, Antti-Jussi Vuotikka
Simulation&Calculation, Global Boiler Works Oy
Lumijoentie 8, 90400 Oulu, Finland
sami.kreivi@gbw.fi, antti-jussi.vuotikka@gbw.fi

Teemu Kuivaniemi, Antti Mäntylä, Joona Vaara,
Jaakko Istolahti, Pasi Halla-aho, Tero Frondelius
R&D and Engineering, Wärtsilä
Teollisuuskatu 9b, 65170 Vaasa, Finland
firstname.lastname@wartsila.com

Tero Frondelius
Materials and Mechanical Engineering, University of Oulu
Pentti Kaiteran katu 1, 90014 Oulu, Finland
firstname.lastname@oulu.fi